

Berry curvature dipole and nonlinear Hall effect in two-dimensional Nb_{2n+1}Si_nTe_{4n+2}Yiwei Zhao^{1,2}, Jin Cao,^{3,2,*} Zeying Zhang,^{4,2,†} Si Li,⁵ Yan Li,¹ Fei Ma,^{1,‡} and Shengyuan A. Yang^{1,2}¹State Key Laboratory for Mechanical Behavior of Materials, Xi'an Jiaotong University, Shaanxi 710049, China²Research Laboratory for Quantum Materials, Singapore University of Technology and Design, Singapore 487372, Singapore³Centre for Quantum Physics, Key Laboratory of Advanced Optoelectronic Quantum Architecture and Measurement (MOE), Beijing Institute of Technology, Beijing 100081, China⁴College of Mathematics and Physics, Beijing University of Chemical Technology, Beijing 100029, China⁵School of Physics, Northwest University, Shaanxi 710127, China

(Received 3 January 2023; accepted 1 May 2023; published 11 May 2023)

Recent experiments have demonstrated interesting physics in a family of two-dimensional composition-tunable materials Nb_{2n+1}Si_nTe_{4n+2}. Here we show that, owing to their intrinsic low symmetry, metallic nature, tunable composition, and ambient stability, these materials offer a good platform for studying the Berry curvature dipole (BCD) and nonlinear Hall effect. Using first-principles calculations, we find that the BCD exhibits pronounced peaks in monolayer Nb₃SiTe₆ (the $n = 1$ case). Its magnitude decreases monotonically with n and completely vanishes in the $n \rightarrow \infty$ limit. This variation manifests a special hidden dimensional crossover of the low-energy electronic states in this system. The resulting nonlinear Hall response from the BCD in these materials is discussed. Our work reveals pronounced geometric quantities and nonlinear transport physics in Nb_{2n+1}Si_nTe_{4n+2} family materials, which should be readily detected in experiment.

DOI: [10.1103/PhysRevB.107.205124](https://doi.org/10.1103/PhysRevB.107.205124)**I. INTRODUCTION**

The Hall effects, in which an antisymmetric contribution j_H to the transverse current is induced by a longitudinal driving E field, are of fundamental importance in condensed-matter physics [1–3]. At linear order, i.e., with $j_H \sim E$, the Hall effect requires the broken time-reversal symmetry \mathcal{T} , which can be achieved either by an applied magnetic field or by intrinsic magnetism. This constraint is loosened when considering Hall responses at nonlinear order, as the nonequilibrium electron distribution driven by the E field already breaks \mathcal{T} at its first order. Focusing on the second-order response, in nonmagnetic materials and in the absence of magnetic field, Sodemann and Fu proposed a Berry curvature dipole (BCD) contribution to the nonlinear Hall current $j_H \sim E^2$ within the semiclassical theory framework [4]. Their work has attracted a great deal of interest in the past few years, and the effect has been successfully detected in several material systems [5–24]. It was suggested that this effect offers a new mechanism for nonlinear applications, such as frequency doubling and rectification [25–27].

For experimental study, two-dimensional (2D) materials have advantages in their great tunability. For example, the Fermi level in 2D materials can be readily tuned via gating technique to a large extent not possible in 3D bulk materials [5,28]. However, regarding the BCD and its induced nonlinear Hall effect, the constraint from crystalline symmetry

in two dimensions is rather stringent. It was shown that in two dimensions, a nonzero BCD is compatible only with a single in-plane mirror line [4]. Explicitly, the allowed wallpaper groups are just $P1$, Pm , Pg , and Cm . Regarding layer groups, there are 19 allowed ones: Nos. 1, 4, 5, 8–13, and 27–36. Hence, to realize the effect, one has to choose crystals with very low symmetry, which are rather limited, or take extra effort to exert strain or twist on the crystal to lower the symmetry. This severely hinders the experimental study.

Recently, the family of composition-tunable materials Nb_{2n+1}Si_nTe_{4n+2} has attracted interest in both theory and experiment [29–34]. In the bulk form, these materials are van der Waals layered materials. Their high-quality 2D layers can be obtained by the mechanical exfoliation method [35]. The special feature of this family is the tunable composition embodied by the integer n [36–39]. For each n , the system is a stoichiometric crystal, and the physical properties have an interesting dependence on n . For example, it was shown that in a 2D monolayer, for finite n , the material is a nonsymmorphic nodal-line semimetal [29], whereas for the $n \rightarrow \infty$ limit, the material, i.e., Nb₂SiTe₄, is a narrow-gap semiconductor [33,40]. With increasing n , the low-energy states at the Fermi level exhibits a dimensional change from 2D-like states to 1D-like states [32].

We note that 2D Nb_{2n+1}Si_nTe_{4n+2} materials actually offer a good platform to explore BCD-related physics. First, except for the $n \rightarrow \infty$ limit, all members of the family have a sufficiently low symmetry to allow an intrinsic BCD, without the need for applied strain. Second, they offer an opportunity for systematic investigation of the evolution of the BCD with the tunable composition. Third, these 2D materials are stable at

* caojin.phy@gmail.com

† zzy@mail.buct.edu.cn

‡ mafei@mail.xjtu.edu.cn

ambient conditions [32], which facilitates experimental study as well as possible applications.

Motivated by the above considerations, in this work we study theoretically the BCD and nonlinear Hall effect in monolayer $\text{Nb}_{2n+1}\text{Si}_n\text{Te}_{4n+2}$ materials. With first-principles calculations, we show that the $n = 1$ case, i.e., Nb_3SiTe_6 , possesses a pronounced BCD. The magnitude can reach 1.54 \AA in the hole-doped case, larger than previously reported values in 2D $T_d\text{-WTe}_2$ [18], strained NbS_2 [21], and WSe_2 [18]. With increasing n , the BCD peaks in the spectrum show a monotonic decrease and eventually vanish in the $n \rightarrow \infty$ limit. This behavior can be understood from two perspectives: One is from the symmetry perspective and the other is from the dimensional evolution of the electronic states. The latter view manifests that although structurally these materials are strongly bonded in both directions in two dimensions, electronically the states exhibit a dimensional crossover from two dimensions to one. This hidden crossover dictates the change in the BCD. The key features of the results are further captured by our tight-binding models constructed for this family of materials. To guide the experiment, we discuss the properties of the nonlinear Hall response arising from the BCD. Our work reveals interesting properties of the $\text{Nb}_{2n+1}\text{Si}_n\text{Te}_{4n+2}$ family materials and suggests them as a suitable platform to explore BCD and nonlinear Hall physics.

II. COMPUTATIONAL METHOD

Our first-principle calculations were based on the density functional theory (DFT), performed by using the VIENNA *ab initio* simulation package [41–43]. The ionic potentials were treated by using the projector augmented wave method [44]. The exchange-correlation functional was treated by the generalized gradient approximation [45] in the scheme by Perdew *et al.* [46]. The plane-wave cutoff energy was set to be 400 eV, and a $10 \times 4 \times 1$ Γ -centered k -point mesh was used for the Brillouin zone (BZ) sampling. The convergence criteria for the total energy and the force were set to be 10^{-6} eV and 0.01 eV/\AA , respectively. To avoid artificial interaction between periodic images, a vacuum space of 20 \AA thickness normal to the 2D layer (i.e., in the z direction) was added. Spin-orbital coupling (SOC) was included in all calculations. Based on the band-structure calculation, an *ab initio* tight-binding model was constructed using the WANNIER90 package [47]. The d orbitals of Nb atoms and p orbitals of Te atoms were used as the initial guess of the local basis. The BCD was calculated based on this *ab initio* tight-binding model. In evaluating the BCD, we set $T = 100 \text{ K}$ in the Fermi distribution function.

III. CRYSTAL AND ELECTRONIC STRUCTURES

The $\text{Nb}_{2n+1}\text{Si}_n\text{Te}_{4n+2}$ family materials were first synthesized by chemical vapor transport method [36]. The lattice structures of their 2D monolayers are illustrated in Fig. 1. Here, each monolayer consists of three atomic layers: The middle layer containing Nb and Si atoms is sandwiched between two Te layers [Fig. 1(a)]. From the top view [see Figs. 1(b)–1(d)], these materials can be seen as composed of three building blocks, which are conventionally called the a , b ,

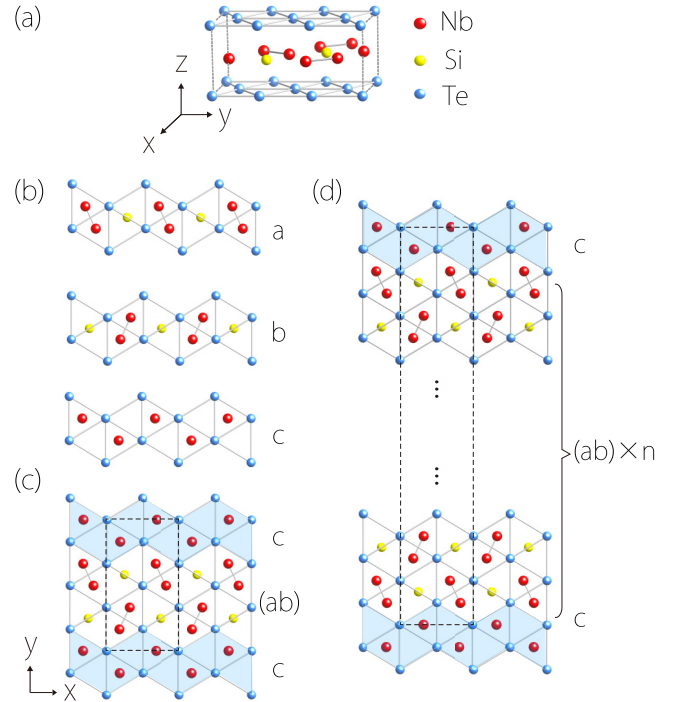


FIG. 1. (a) Lattice structure of monolayer Nb_3SiTe_6 . (b) The three building blocks of $\text{Nb}_{2n+1}\text{Si}_n\text{Te}_{4n+2}$ family materials: a , b , and c chains. (c) Top view of the $n = 1$ case (Nb_3SiTe_6). The dashed box marks the unit cell. (d) $\text{Nb}_{2n+1}\text{Si}_n\text{Te}_{4n+2}$ can be constructed by n copies of (ab) chains and one c chain in a unit cell (the dashed box).

and c chains. As shown in Fig. 1(b), a and b chains contain Si atoms and have the same composition as $\text{NbSi}_{1/2}\text{Te}_2$, whereas the c chain does not contain Si and has the composition of NbTe_2 . Assuming these chains are along the x direction [as in Fig. 1(c)], then a and b are connected by a glide mirror operation $\hat{M}_y = \{M_y | \frac{1}{2}0\}$, and in these materials they always appear together. Members of this family are formed by assembling these chains along the lateral direction (y) in a periodic manner such that $\text{Nb}_{2n+1}\text{Si}_n\text{Te}_{4n+2}$ corresponds to the arrangement of $(ab)_n c$. Namely, in a period, we have one c chain and n copies of (ab) chains, as illustrated in Fig. 1(d). In the $n = \infty$ limit, there is no c chain in the structure anymore and we reach the composition of Nb_2SiTe_4 .

Our optimized lattice parameters for $n = 1, 2, 3, \infty$ are listed in Table I. These values are in good agreement with experiment and previous calculations [29,30,32]. We also note that for members with finite n , they all have the layer group symmetry $Pb2_1m$, with C_{2v} point group. In comparison,

TABLE I. Optimized lattice parameters and the corresponding symmetries of representative monolayer $\text{Nb}_{2n+1}\text{Si}_n\text{Te}_{4n+2}$ materials.

n	a (\AA)	b (\AA)	Thickness (\AA)	Layer group	Point group
1	6.408	11.633	3.649	$Pb2_1m$	C_{2v}
2	6.405	19.590	3.770	$Pb2_1m$	C_{2v}
3	6.404	27.552	3.651	$Pb2_1m$	C_{2v}
∞	6.401	7.962	3.783	$Pbam$	D_{2h}

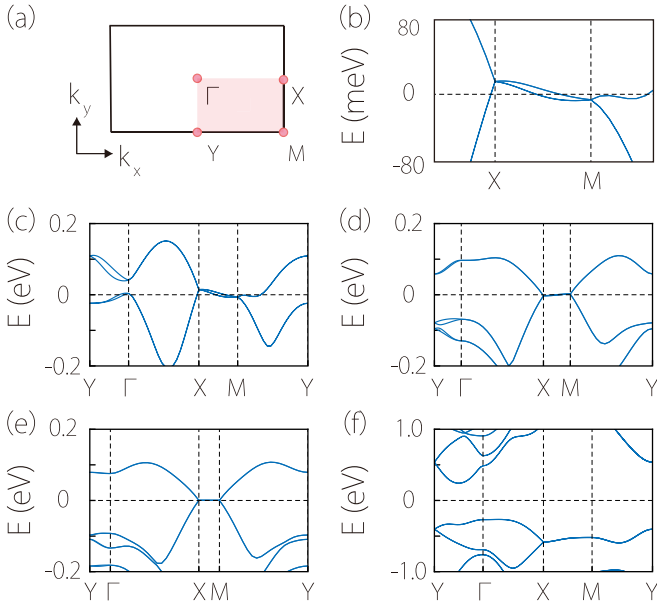


FIG. 2. (a) Brillouin zone for monolayer $\text{Nb}_{2n+1}\text{Si}_n\text{Te}_{4n+2}$. (b)–(f) Band structures for monolayer $\text{Nb}_{2n+1}\text{Si}_n\text{Te}_{4n+2}$: (b) and (c) $n = 1$, with (b) a close-up around the path X - M in (c); (d) $n = 2$; (e) $n = 3$; and (f) $n = \infty$.

Nb_2SiTe_4 with $n = \infty$ has a larger layer group $Pbam$ and a point group D_{2h} . The main difference is the extra glide mirror $\tilde{M}_x = \{M_x | 0\frac{1}{2}\}$ for the $n = \infty$ case but not for any finite n . From Fig. 1(c) one can see that it is the c chains that break the \tilde{M}_x symmetry which holds for (ab) chains.

In Fig. 2 we plot the calculated electronic band structures for the four representative members in Table I (band structures in a larger energy window are also presented in the Supplemental Material [48]). One can see that the band structures for $n = 1, 2, 3$ show similar features. Previous works have shown that in the absence of SOC, these materials are nodal-line semimetals [29,32]. The nodal line on the X - M path around the Fermi level is enforced by the nonsymmorphic $\mathcal{T}\tilde{M}_y$ symmetry. The detailed analysis was given in our previous works [49], so we will not repeat it here. It should be noted that in Fig. 2, the band structures include the SOC effects. Under SOC, the $\mathcal{T}\tilde{M}_y$ symmetry protection is no longer exact, so the original nodal-line degeneracy will be lifted. In the enlarged view in Fig. 2(b), one can clearly see the splitting of the nodal line. Nevertheless, there is still a degenerate nodal point at X (and also at M). This point is a fourfold-degenerate Dirac point enforced by nonsymmorphic symmetries of the system. Its formation mechanism was discussed in Ref. [29]. The SOC-induced change to the band structure is weak, so for many properties, SOC may just be neglected. However, band geometric properties like Berry curvature and the BCD are very sensitive to small-gap regions in band structures, such as those due to SOC splitting. Therefore, to study the BCD and its nonlinear Hall effect, we have to include SOC in the calculation.

The low-energy states around the Fermi level are mostly distributed on the c chains. Previous scanning tunneling spectroscopy experiments also verified this feature [32,33]. With increasing n , the distance between two c chains will increase

and hence the coupling between them will decrease. As a result, the band dispersion will become flatter along the y direction, as can be seen in Figs. 2(c)–2(e) along the Γ - Y and X - M paths.

For Nb_2SiTe_4 with $n = \infty$, Fig. 2(f) shows that it is a narrow-gap semiconductor. The band gap is approximately 0.51 eV, which is slightly larger than the band gap of layered Nb_2SiTe_4 (approximately 0.39 eV) [40]. This different character can now be understood from the discussion above. One can view the c chains as metals, whereas the (ab) chains are insulating. Since Nb_2SiTe_4 is entirely made of (ab) chains, its spectrum would naturally be gapped.

The features discussed above, particularly the evolution of the band structure with n , will have important implications for the BCD and nonlinear Hall response in these materials.

IV. BERRY CURVATURE DIPOLE

Berry curvature is an intrinsic band geometric quantity. It plays an important role in many physical properties, especially anomalous transport properties [50]. In nonmagnetic materials, nonzero Berry curvature requires the breaking of inversion symmetry. This condition is fulfilled in monolayer $\text{Nb}_{2n+1}\text{Si}_n\text{Te}_{4n+2}$ with finite n . For Nb_2SiTe_4 with $n = \infty$, inversion symmetry is respected and hence Berry curvature vanishes identically.

For a 2D system, Berry curvature only has a single component, which can be expressed as (we set $e = \hbar = 1$ in the formulas)

$$\Omega_z(n\mathbf{k}) = -2 \text{Im} \sum_{n' \neq n} \frac{\langle u_{n\mathbf{k}} | v_x | u_{n'\mathbf{k}} \rangle \langle u_{n'\mathbf{k}} | v_y | u_{n\mathbf{k}} \rangle}{(\varepsilon_{n\mathbf{k}} - \varepsilon_{n'\mathbf{k}})^2} \quad (1)$$

for a state $|u_{n\mathbf{k}}\rangle$, where v_x and v_y are the velocity operators and $\varepsilon_{n\mathbf{k}}$ is the energy of $|u_{n\mathbf{k}}\rangle$. Consider Nb_3SiTe_6 ($n = 1$). In Fig. 3(a) we plot the distribution of its Berry curvature in the BZ for occupied states, i.e., the quantity

$$\Omega(\mathbf{k}) = \sum_n f_0(n\mathbf{k}) \Omega_z(n\mathbf{k}), \quad (2)$$

where f_0 is the Fermi distribution function. One observes that the Berry curvature is odd in k_y and even in k_x , as required by \mathcal{T} and \tilde{M}_y , and its value is quite pronounced along the Γ - Y path.

The BCD is the first moment of Berry curvature in the BZ. It is a pseudovector in two dimensions, defined as [4]

$$\begin{aligned} \mathcal{D}_a &= \sum_n \int_{\text{BZ}} \frac{d^2k}{(2\pi)^2} f_0(n\mathbf{k}) \partial_a \Omega_z(n\mathbf{k}) \\ &= - \sum_n \int_{\text{BZ}} \frac{d^2k}{(2\pi)^2} f_0'(n\mathbf{k}) v_a(n\mathbf{k}) \Omega_z(n\mathbf{k}), \end{aligned} \quad (3)$$

where $a \in \{x, y\}$ and $\partial_a \equiv \partial_{k_a}$. In the second line, we performed an integration by parts, which explicitly demonstrates that the BCD is a Fermi surface property.

For finite n , $\text{Nb}_{2n+1}\text{Si}_n\text{Te}_{4n+2}$ only has a single mirror line along x , which allows a nonzero BCD. Since \mathcal{D} is a pseudovector, it must be along the y direction, i.e., $\mathcal{D} = \mathcal{D}_y \hat{y}$. In Fig. 3(b) we plot the calculated \mathcal{D}_y versus the chemical potential μ for $n = 1$. One observes two peaks in the figure:

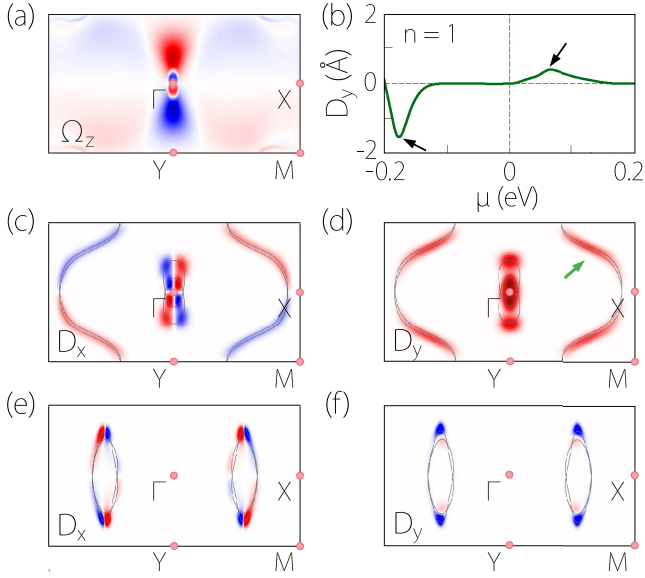


FIG. 3. Berry curvature and its dipole in Nb_3SiTe_6 . (a) Distribution of Berry curvature for the occupied states. (b) The BCD \mathcal{D}_y versus chemical potential μ . (c)–(f) The k -resolved BCD as defined in Eq. (4), plotted for (c) and (d) $\mu = 0.064$ eV [the upper peak in (b)] and (e) and (f) $\mu = -0.180$ eV [the lower peak in (b)]. The Fermi contours at these energies are indicated by the black curves.

One is at 0.064 eV with a value of 0.399 Å and the other is at -0.180 eV with a value of -1.540 Å. The two peaks are of opposite signs. We note that the magnitude of -1.540 Å is quite large. This is comparable to or larger than those found in monolayer T_d - WTe_2 (0.1 – 0.7 Å) [18], strained NbS_2 (0.2 Å) [21], and strained WSe_2 (0.02 Å) [18].

To understand the origin of the large BCD in monolayer Nb_3SiTe_6 , we plot the momentum space distribution of the quantity

$$\mathcal{D}_a(\mathbf{k}) = - \sum_n f'_0(n\mathbf{k}) v_a(n\mathbf{k}) \Omega_z(n\mathbf{k}), \quad (4)$$

which, according to Eq. (3), represents the k -resolved contribution to the BCD (on the Fermi surface). In Figs. 3(c)–3(f) the plots are made for $\mu = 0.064$ eV (upper peak) and -0.180 eV (lower peak). First of all, one observes that $\mathcal{D}_x(\mathbf{k})$ is an odd function in k_y whereas $\mathcal{D}_y(\mathbf{k})$ is an even function, as required by the \tilde{M}_y symmetry. Hence, after integration over the BZ, the BCD only has the y component left. From Figs. 3(c)–3(f) one can see that the nodal-line region along X – M does not make a sizable contribution to the BCD. For the upper peak [Fig. 3(d)], the large contribution to \mathcal{D}_y is from the Γ – Y path, which corresponds to the SOC splitting gap indicated in Fig. 2(c). The spin splitting gap on the outer Fermi surface [marked by the green arrow in Fig. 3(d)] also gives a non-negligible contribution. As for the lower peak, Figs. 3(e) and 3(f) show that the Fermi surface has two separate pieces. By examining the band structure around the hot spots in Fig. 3(f), we find that the large negative contribution is also from SOC splitting of the band structure.

Next we consider the cases with $n = 2$ and 3 . From the results in Fig. 4 one can see that the magnitude of the BCD

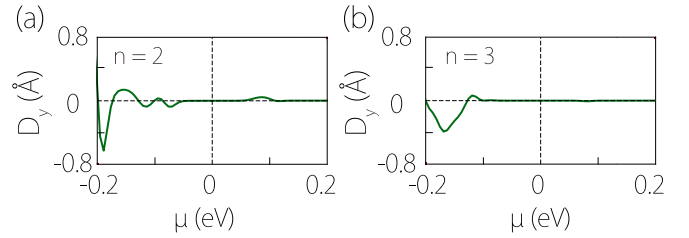


FIG. 4. The BCD \mathcal{D}_y versus chemical potential μ for the (a) $n = 2$ and (b) $n = 3$ cases.

decreases with increasing n . For $n = 3$, the BCD value above $\mu = 0$ (which is also the energy of the nodal line) is already negligibly small. As for the lower peak, the value is about 0.663 Å for $n = 2$ and 0.396 Å for $n = 3$.

This trend of a decreasing BCD with increasing n in monolayer $\text{Nb}_{2n+1}\text{Si}_n\text{Te}_{4n+2}$ can be understood from two perspectives. First, in terms of symmetry, $\text{Nb}_{2n+1}\text{Si}_n\text{Te}_{4n+2}$ with finite n supports the BCD because of its low symmetry. The presence of c chains is crucial because they break the \tilde{M}_x symmetry of (ab) chains (Fig. 5). Without c chains, \tilde{M}_x becomes an exact symmetry and it suppresses the BCD (given the other mirrors in the system) as in the $n = \infty$ limit. Hence, the density of c chains in the system can be viewed as a measure of the extent of symmetry breaking. It is strongest in the $n = 1$ case and gradually decreases as n increases, determining the trend in the BCD.

Meanwhile, the trend is also connected with the dimensional crossover in this system [34]. As discussed, the low-energy states are mostly distributed on the c chains. One may view the c chains as metallic 1D subsystems put in an insulating matrix formed by the (ab) chains. For small n , the system retains a 2D character, because the c chains are not far from each other and the interchain coupling is sizable. However, with increasing n , the interchain coupling will decrease and the system approaches the quasi-1D character. Berry curvature is a differential 2-form, which vanishes in the 1D limit [as can also be seen from Eq. (1)]. Thus, the BCD

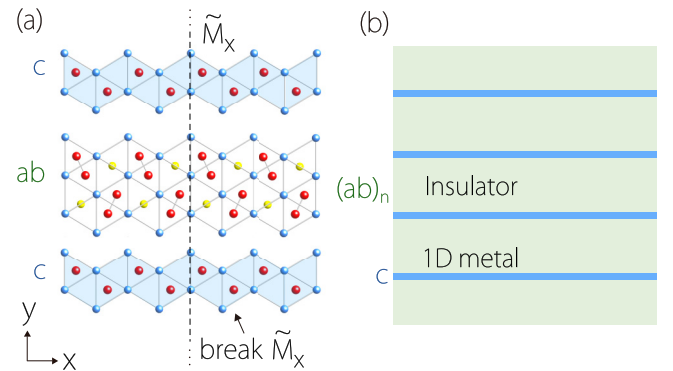


FIG. 5. (a) The (ab) chains preserve the \tilde{M}_x symmetry, whereas c chains break it. Hence, the density of c chains represents the extent of \tilde{M}_x symmetry breaking. (b) The $\text{Nb}_{2n+1}\text{Si}_n\text{Te}_{4n+2}$ system may be schematically viewed as 1D metallic chains (c chains) embedded in a 2D insulator matrix [made of (ab) chains].

must decrease and approach zero during this dimensional crossover.

It must be emphasized that the dimensional crossover here refers to the low-energy electronic states. Structurally, $\text{Nb}_{2n+1}\text{Si}_n\text{Te}_{4n+2}$ materials always maintain a 2D material character: The lattices are strongly bonded in both the x and y directions. Thus, the crossover is a hidden feature that occurs only for the electronic sector. This is a very interesting piece of physics for 2D $\text{Nb}_{2n+1}\text{Si}_n\text{Te}_{4n+2}$ materials. Now we reveal its manifestation in the BCD, which can be detected via nonlinear Hall measurement.

V. MODEL STUDY

To understand the features in the band structure and in the BCD, we construct a minimal lattice model to describe the low-energy bands in monolayer $\text{Nb}_{2n+1}\text{Si}_n\text{Te}_{4n+2}$ with finite n . The model may also serve as a good starting point for subsequent theoretical studies of this class of materials.

In Refs. [34,49] we proposed a 2D Dirac Su-Schrieffer-Heeger (SSH) model, which is spinless (i.e., without SOC) and captures the nonsymmorphic nodal-line feature in monolayer $\text{Nb}_{2n+1}\text{Si}_n\text{Te}_{4n+2}$. However, to study the BCD, as we noted, the consideration of SOC is necessary. Therefore, we need to extend the previous spinless Dirac SSH model to include SOC effects.

The Dirac SSH model is defined on a rectangular lattice, as shown in Fig. 6. It consists of an array of zigzag chains running in the x direction. In a unit cell, there are two sites A and B . Physically, each chain corresponds to a c chain in $\text{Nb}_{2n+1}\text{Si}_n\text{Te}_{4n+2}$. The construction is motivated by the DFT results showing that the low-energy bands are mainly from the d_{z^2} orbitals on the Nb sites in c chains. Assigning one orbital to each site and considering the nearest intrachain and interchain hoppings, one obtains the model constrained by \mathcal{T} , \tilde{M}_y , and M_z symmetries,

$$\begin{aligned} \mathcal{H}_0 = & t \begin{bmatrix} 0 & 1 + e^{-ik_x} \\ 1 + e^{ik_x} & 0 \end{bmatrix} \sigma_0 \\ & + t' \begin{bmatrix} 0 & e^{-ik_y}(1 + e^{-ik_x}) \\ e^{ik_y}(1 + e^{ik_x}) & 0 \end{bmatrix} \sigma_0, \end{aligned} \quad (5)$$

where the momenta are measured in units of the lattice constant inverses and the Pauli matrices σ denote the spin degree of freedom.

Next we add SOC to the model. The above-mentioned symmetries result in the following SOC terms up to next-nearest-neighbor hopping processes:

$$\begin{aligned} \mathcal{H}_{\text{SOC}} = & t \begin{bmatrix} 2\lambda_1 \sin k_x & 0 \\ 0 & -2\lambda_1 \sin k_x \end{bmatrix} \sigma_z \\ & + t' \begin{bmatrix} 2\lambda_3 \sin k_y & i\lambda_2 e^{ik_y}(1 + e^{-ik_x}) \\ -i\lambda_2 e^{-ik_y}(1 + e^{ik_x}) & 2\lambda_3 \sin k_y \end{bmatrix} \sigma_z. \end{aligned} \quad (6)$$

Here the first term is from the intrachain hopping process, whereas the second term is from the interchain process, as indicated in Fig. 6(b). Therefore, our spin-orbit-coupled Dirac SSH model is obtained as

$$\mathcal{H} = \mathcal{H}_0 + \mathcal{H}_{\text{SOC}}. \quad (7)$$

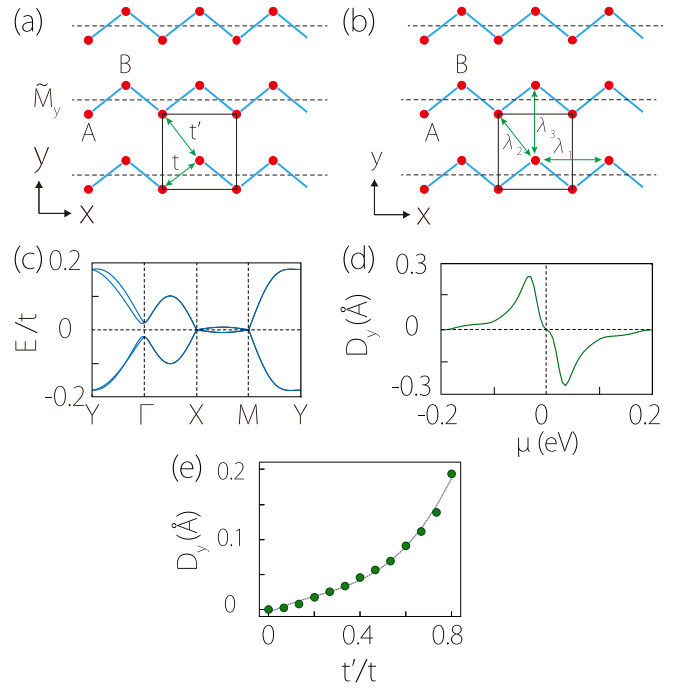


FIG. 6. (a) Schematic showing the tight-binding model. The model consists of zigzag chains. A primitive cell contains two sites A and B ; t and t' are the amplitudes for intrachain and interchain hoppings, respectively. (b) Three hopping processes corresponding to the SOC terms in Eq. (6). (c) Band structure of the tight-binding model. (d) Corresponding BCD \mathcal{D}_y versus chemical potential. (e) Variation of the BCD peak value as a function of the interchain coupling. The solid curve is a guide to the eye. In (c) and (d) we set $t = 0.2$ eV, $t' = 0.16$ eV, $\lambda_1 = 1$, and $\lambda_2 = \lambda_3 = 0.1$. The same values of t and λ are taken in (e).

In Fig. 6(c) we plot a typical band structure of this model. Namely, there is an approximate nodal line on the X - M path (split by SOC); the SOC splitting is observed on the X - M and Y - Γ paths, but not on the Γ - X and M - Y paths. The double degeneracy on X - M and Y - Γ is due to the anticommution between \tilde{M}_y and M_z on these two paths. One can see that it indeed captures the main features of DFT band structures in Fig. 2(c). In Fig. 6(c) we plot the BCD calculated for this model. The two BCD peaks in Fig. 3(b) are reproduced in this simple model. One peak is above the nodal-line energy and the other one is below, and they have opposite signs. Finally, we plot the BCD peak magnitude as a function of interchain coupling t' . One can see that the value monotonically increases with the interchain coupling. Since t' decreases with n in monolayer $\text{Nb}_{2n+1}\text{Si}_n\text{Te}_{4n+2}$, the behavior in Fig. 6(d) agrees with our result from DFT calculations.

VI. NONLINEAR HALL EFFECT

It was shown that the BCD leads to a second-order nonlinear Hall current. For a 2D system, the current can be expressed as

$$\mathbf{j}_H = -\frac{1}{2}\tau \hat{z} \times \mathbf{E}(\mathcal{D} \cdot \mathbf{E}), \quad (8)$$

where \mathbf{E} is the applied in-plane E field and τ is the relaxation time. Consider monolayer $\text{Nb}_{2n+1}\text{Si}_n\text{Te}_{4n+2}$ with the

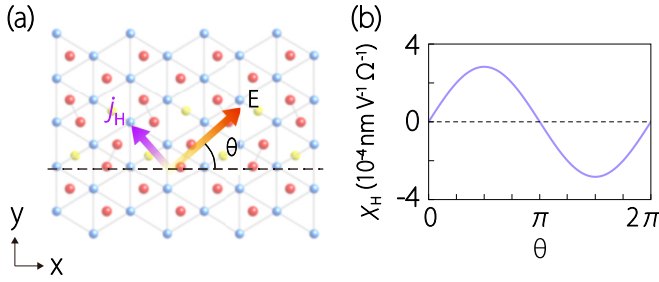


FIG. 7. (a) Nonlinear Hall current induced by the E field in Nb_3SiTe_6 . The in-plane E field makes an angle θ with the mirror line. The induced Hall current is perpendicular to the E field, as indicated by the green arrow. (b) Nonlinear Hall conductivity χ_H versus the angle θ .

coordinate setup in Fig. 7(a). Assuming the applied E field is in the direction specified by the polar angle θ (with respect to the mirror line), i.e., $(E_x, E_y) = E(\cos\theta, \sin\theta)$, the Hall current will be in the direction of $(j_x, j_y) = j_H(-\sin\theta, \cos\theta)$, with the Hall current magnitude

$$j_H = \chi_H(\theta)E^2 \quad (9)$$

and the nonlinear Hall conductivity

$$\chi_H(\theta) = -\frac{1}{2}\tau\mathcal{D}_y \sin\theta. \quad (10)$$

Experimentally, a 2D material sample can be etched into a disk shape and attached with multiple pairs of leads [6,51] such that the $\sin\theta$ angular dependence in the nonlinear Hall response can be verified in experiment. To measure the second-order nonlinear response, one typically modulates the driving source with a low frequency and detects the signal at double frequency using the lock-in technique [5,6]. The Fermi level of 2D materials can be readily tuned by using the electric gating technique. Here consider monolayer Nb_3SiTe_6 (i.e., $n = 1$). With our calculated $\mathcal{D}_y \sim 1.54 \text{ \AA}$ at the lower peak, assuming $\tau = 10 \text{ ps}$, which is typical for 2D materials, the magnitude of χ_H can reach $2.9 \times 10^{-4} \text{ nm S/V}$ and its angular dependence is shown in Fig. 7(b). Under a driving field of $E \sim 10^4 \text{ V/m}$, the resulting nonlinear Hall current density

can reach approximately $0.6 \mu\text{A/cm}$. For $n = 2$ (3), the signal is expected to be smaller by a factor of approximately 2 (approximately 4), which is still detectable in experiment.

VII. CONCLUSION

We have revealed monolayer $\text{Nb}_{2n+1}\text{Si}_n\text{Te}_{4n+2}$ materials as a suitable platform for studying the BCD and nonlinear Hall effect. These materials have adequate symmetry to support the effect without extra strain, enjoy stability at ambient conditions, and exhibit composition tunability. We showed that the BCD is most pronounced for the $n = 1$ case, where its magnitude can reach 1.54 \AA . The BCD value decreases with increasing n . This can be understood from the degree of symmetry breaking and also from a dimensional crossover. It is interesting that this crossover occurs only for the low-energy electronic states, whereas structurally the system is always strongly bonded in two dimensions. The evolution of the BCD with n can be regarded as a manifestation of this hidden transition. We constructed the spin-orbit-coupled Dirac SSH model, which captures the main features of the DFT results. The nonlinear Hall conductivity and its angular dependence were analyzed. Our work uncovered interesting geometric quantities and nonlinear physics in the $\text{Nb}_{2n+1}\text{Si}_n\text{Te}_{4n+2}$ family materials. It provides useful guidance for subsequent experiments on these systems.

ACKNOWLEDGMENTS

The authors thank D. L. Deng for helpful discussions. This work was supported by Singapore Ministry of Education AcRF Tier 2 (Grant No. T2EP50220-0026), National Natural Science Foundation of China (Grants No. 52271136, No. 11704304, and No. 12204378), and Natural Science Foundation of Shaanxi Province (Grants No. 2019TD-020, No. 2019JLM-30, No. 2017JZ015, and No. 2018JQ1028). The computing for this work was performed at the High Performance Computing Center at Xi'an Jiaotong University. Z.Z. acknowledges the support by the NSF of China (Grant No. 12004028).

-
- [1] K. von Klitzing, *Rev. Mod. Phys.* **58**, 519 (1986).
[2] N. Nagaosa, J. Sinova, S. Onoda, A. H. MacDonald, and N. P. Ong, *Rev. Mod. Phys.* **82**, 1539 (2010).
[3] J. Sinova, S. O. Valenzuela, J. Wunderlich, C. H. Back, and T. Jungwirth, *Rev. Mod. Phys.* **87**, 1213 (2015).
[4] I. Sodemann and L. Fu, *Phys. Rev. Lett.* **115**, 216806 (2015).
[5] Q. Ma, S.-Y. Xu, H. Shen, D. MacNeill, V. Fatemi, T.-R. Chang, A. M. Mier Valdivia, S. Wu, Z. Du, C.-H. Hsu, S. Fang, Q. D. Gibson, K. Watanabe, T. Taniguchi, R. J. Cava, E. Kaxiras, H.-Z. Lu, H. Lin, L. Fu, N. Gedik, and P. Jarillo-Herrero, *Nature (London)* **565**, 337 (2019).
[6] K. Kang, T. Li, E. Sohn, J. Shan, and K. F. Mak, *Nat. Mater.* **18**, 324 (2019).
[7] J. Son, K.-H. Kim, Y. H. Ahn, H.-W. Lee, and J. Lee, *Phys. Rev. Lett.* **123**, 036806 (2019).
[8] R. Battilomo, N. Scopigno, and C. Ortix, *Phys. Rev. Lett.* **123**, 196403 (2019).
[9] J. Kim, K.-W. Kim, D. Shin, S.-H. Lee, J. Sinova, N. Park, and H. Jin, *Nat. Commun.* **10**, 3965 (2019).
[10] S. Dzsaber, X. Yan, M. Taupin, G. Eguchi, A. Prokofiev, T. Shiroka, P. Blaha, O. Rubel, S. E. Grefe, H.-H. Lai, Q. Si, and S. Paschen, *Proc. Natl. Acad. Sci. U.S.A.* **118**, e2013386118 (2021).
[11] P. He, H. Isobe, D. Zhu, C.-H. Hsu, L. Fu, and H. Yang, *Nat. Commun.* **12**, 698 (2021).
[12] M.-S. Qin, P.-F. Zhu, X.-G. Ye, W.-Z. Xu, Z.-H. Song, J. Liang, K. Liu, and Z.-M. Liao, *Chin. Phys. Lett.* **38**, 017301 (2021).
[13] M. Huang, Z. Wu, J. Hu, X. Cai, E. Li, L. An, X. Feng, Z. Ye, N. Lin, K. T. Law, and N. Wang, *Natl. Sci. Rev.* **nwac232** (2022).
[14] C.-L. Zhang, T. Liang, Y. Kaneko, N. Nagaosa, and Y. Tokura, *npj Quantum Mater.* **7**, 103 (2022).
[15] S. Sinha, P. C. Adak, A. Chakraborty, K. Das, K. Debnath, L. D. V. Sangani, K. Watanabe, T. Taniguchi, U. V. Waghmare, A. Agarwal, and M. M. Deshmukh, *Nat. Phys.* **18**, 765 (2022).

- [16] Z. Z. Du, C. M. Wang, H.-Z. Lu, and X. C. Xie, *Phys. Rev. Lett.* **121**, 266601 (2018).
- [17] Y. Zhang, Y. Sun, and B. Yan, *Phys. Rev. B* **97**, 041101(R) (2018).
- [18] J.-S. You, S. Fang, S.-Y. Xu, E. Kaxiras, and T. Low, *Phys. Rev. B* **98**, 121109(R) (2018).
- [19] Y. Zhang, J. van den Brink, C. Felser, and B. Yan, *2D Mater.* **5**, 044001 (2018).
- [20] J. I. Facio, D. Efremov, K. Koepernik, J.-S. You, I. Sodemann, and J. van den Brink, *Phys. Rev. Lett.* **121**, 246403 (2018).
- [21] R.-C. Xiao, D.-F. Shao, Z.-Q. Zhang, and H. Jiang, *Phys. Rev. Appl.* **13**, 044014 (2020).
- [22] C. Zeng, S. Nandy, and S. Tewari, *Phys. Rev. B* **103**, 245119 (2021).
- [23] D. Wawrzik, J.-S. You, J. I. Facio, J. van den Brink, and I. Sodemann, *Phys. Rev. Lett.* **127**, 056601 (2021).
- [24] Z. Du, H.-Z. Lu, and X. Xie, *Nat. Rev. Phys.* **3**, 744 (2021).
- [25] G. Pacchioni, *Nat. Rev. Mater.* **4**, 514 (2019).
- [26] Y. Zhang and L. Fu, *Proc. Natl. Acad. Sci. U.S.A.* **118**, e2100736118 (2021).
- [27] D. Kumar, C.-H. Hsu, R. Sharma, T.-R. Chang, P. Yu, J. Wang, G. Eda, G. Liang, and H. Yang, *Nat. Nanotechnol.* **16**, 421 (2021).
- [28] J. Chen, H. J. Qin, F. Yang, J. Liu, T. Guan, F. M. Qu, G. H. Zhang, J. R. Shi, X. C. Xie, C. L. Yang, K. H. Wu, Y. Q. Li, and L. Lu, *Phys. Rev. Lett.* **105**, 176602 (2010).
- [29] S. Li, Y. Liu, S.-S. Wang, Z.-M. Yu, S. Guan, X.-L. Sheng, Y. Yao, and S. A. Yang, *Phys. Rev. B* **97**, 045131 (2018).
- [30] T. Sato, Z. Wang, K. Nakayama, S. Souma, D. Takane, Y. Nakata, H. Iwasawa, C. Cacho, T. Kim, T. Takahashi, and Y. Ando, *Phys. Rev. B* **98**, 121111(R) (2018).
- [31] T. Y. Yang, Q. Wan, D. Y. Yan, Z. Zhu, Z. W. Wang, C. Peng, Y. B. Huang, R. Yu, J. Hu, Z. Q. Mao, S. Li, S. A. Yang, H. Zheng, J. F. Jia, Y. G. Shi, and N. Xu, *Nat. Mater.* **19**, 27 (2020).
- [32] Z. Zhu, S. Li, M. Yang, X.-A. Nie, H.-K. Xu, X. Yang, D.-D. Guan, S. Wang, Y.-Y. Li, C. Liu, Z.-Q. Mao, N. Xu, Y. Yao, S. A. Yang, Y.-G. Shi, H. Zheng, and J.-F. Jia, *npj Quantum Mater.* **5**, 35 (2020).
- [33] B. Wang, W. Xia, S. Li, K. Wang, S. A. Yang, Y. Guo, and J. Xue, *ACS Nano* **15**, 7149 (2021).
- [34] J. Zhang, Y. Lv, X. Feng, A. Liang, W. Xia, S.-K. Mo, C. Chen, J. Xue, S. A. Yang, L. Yang, Y. Guo, Y. Chen, Y. Chen, and Z. Liu, *npj Quantum Mater.* **7**, 54 (2022).
- [35] J. Hu, X. Liu, C. L. Yue, J. Y. Liu, H. W. Zhu, J. B. He, J. Wei, Z. Q. Mao, L. Y. Antipina, Z. I. Popov, P. B. Sorokin, T. J. Liu, P. W. Adams, S. M. A. Radmanesh, L. Spinu, H. Ji, and D. Natelson, *Nat. Phys.* **11**, 471 (2015).
- [36] J. Li, M. E. Badding, and F. DiSalvo, *J. Alloys Compd.* **184**, 257 (1992).
- [37] L. Monconduit, M. Evain, R. Brec, J. Rouxel, and E. Canadell, *Comptes Rendus Acad. Sci. Ser. II* **316**, 25 (1993).
- [38] M. Evain, A. van der Lee, L. Monconduit, and V. Petricek, *Chem. Mater.* **6**, 1776 (1994).
- [39] A. Van der Lee, M. Evain, L. Monconduit, R. Brec, and S. Van Smaalen, *J. Phys.: Condens. Matter* **6**, 933 (1994).
- [40] M. Zhao, W. Xia, Y. Wang, M. Luo, Z. Tian, Y. Guo, W. Hu, and J. Xue, *ACS Nano* **13**, 10705 (2019).
- [41] G. Kresse and J. Hafner, *Phys. Rev. B* **47**, 558 (1993).
- [42] G. Kresse and J. Furthmüller, *Comput. Mater. Sci.* **6**, 15 (1996).
- [43] G. Kresse and J. Furthmüller, *Phys. Rev. B* **54**, 11169 (1996).
- [44] P. E. Blöchl, *Phys. Rev. B* **50**, 17953 (1994).
- [45] J. P. Perdew, J. A. Chevary, S. H. Vosko, K. A. Jackson, M. R. Pederson, D. J. Singh, and C. Fiolhais, *Phys. Rev. B* **46**, 6671 (1992).
- [46] J. P. Perdew, K. Burke, and M. Ernzerhof, *Phys. Rev. Lett.* **77**, 3865 (1996).
- [47] A. A. Mostofi, J. R. Yates, G. Pizzi, Y.-S. Lee, I. Souza, D. Vanderbilt, and N. Marzari, *Comput. Phys. Commun.* **185**, 2309 (2014).
- [48] See Supplemental Material at <http://link.aps.org/supplemental/10.1103/PhysRevB.107.205124> for the calculated band structures with different vacuum gaps and the calculated band structures in a larger energy window.
- [49] J. Cao, H.-R. Chang, X. Feng, Y. Yao, and S. A. Yang, *Phys. Rev. B* **107**, 115168 (2023).
- [50] D. Xiao, M.-C. Chang, and Q. Niu, *Rev. Mod. Phys.* **82**, 1959 (2010).
- [51] S. Lai, H. Liu, Z. Zhang, J. Zhao, X. Feng, N. Wang, C. Tang, Y. Liu, K. S. Novoselov, S. A. Yang, and W.-b. Gao, *Nat. Nanotechnol.* **16**, 869 (2021).